Rotor drop and following thermal growth simulations using detailed auxiliary bearing and damper models

Guangyoung Sun*

NASA, Glenn Research Center, 21000 Brookpark Rd., Cleveland, OH 44135, USA

Abstract

Catcher bearings (CBs) or auxiliary bearings provide mechanical backup protection in the events of magnetic bearing failure. This paper presents numerical analysis for a rotor drop on CBs and following thermal growths due to their mechanical rub using detailed CB and damper models. The detailed CB model is determined based on its material, geometry, speed and preload using the nonlinear Hertzian load–deflection formula, and the thermal growths of bearing components during the rotor drop are estimated using a 1D thermal model. A finite-element squeeze film damper provides the pressure profile of an annular oil film and the resulting viscous damping force. Numerical simulations of an energy storage flywheel with magnetic suspensions failed reveal that an optimal CB design using the detailed simulation models stabilizes the rotor drop dynamics and lowers the thermal growths while preventing the high-speed backward whirl. Furthermore, CB design guides based on the simulation results are presented.
© 2005 Elsevier Ltd. All rights reserved.

1. Introduction

Active magnetic bearings (AMBs) have many advantages over conventional mechanical bearings. In addition to supporting the high-speed rotor without any mechanical friction and lubrication, they enable rotor position and induced vibration to be monitored and controlled by adjusting support stiffness and damping. However, the CBs of rolling-element type are necessary for backup protection since an AMB system employs a feedback loop.

---

*Corresponding author. 20100 Lorain Rd. No. 521, Fairview, OH 44126, USA. Tel.: +1 216 433 6071.
E-mail address: guangdol@hotmail.com.

Kirk et al. [1–4] published several papers regarding rotor drop simulation and CB design in both numerical and experimental ways. They [1,2] studied the influence of support damping on the displacement of the disk and on the rotor/CB contact force using a linear stiffness and damper and showed an optimum damping. Rotor drop tests were conducted for balanced and unbalanced rotors in Ref. [3,4] and it was concluded that a major influence on the transient response is the balance level of the rotor. Swanson et al. [5] provided the test results for 38 rotor drops with varying rotor speed, unbalance amplitude and location for the 5 CB configurations. Chen et al. [6] designed the zero clearance auxiliary bearing and presented its performance over conventional CBs. Xie and Flowers [7] numerically investigated the steady-state behavior of a rotor on CB and studied the effects of various parametric configurations: rotor imbalance, support stiffness and damping. Wang and Noah [8] analyzed the steady-state response of a rigid rotor in a positive-clearance bush using the fixed-point algorithm and predicted a chaotic whirling of the rotor depending on excitation frequency.

Cole et al. [9] developed a deep groove CB model with the elastic deformation of the inner race, which was modeled as a series of flexible beams and studied parametric effects of impact force, bearing width and inner race speed on ball load distributions. However, they did not conduct a rotor drop simulation. Sun et al. [10] introduced an accurate CB stiffness depending on preload and speed but used a linear damper model without considering thermal growth.

For CB applications, most previous researchers have utilized simple CB models using a linear stiffness and damping, and have done little work regarding CB thermal growths. Shin [11] showed, for a non-CB application, that the axial and radial stiffness of a ball bearing decreases substantially as the operating speed increases. Jorgensen and Shin [12] developed a quasi-static bearing model including thermal expansions for a high-speed spindle system.

Detailed bearing and damper models play a significant role in predicting the rotor behavior on CBs accurately, and an estimate of thermal growths during the touchdown is a key CB design factor. In this paper is utilized a detailed ball bearing model [10], which is obtained from load equilibrium equations including the Hertzian contact load between each ball and race, and a finite-element squeeze film damper (FE SFD) determines the pressure distribution of an annular oil film and the resulting viscous damping forces. A 1D CB thermal model composed of heat transfer network and heat sources provides an estimate of thermal growths of the bearing components. The detailed bearing and damper models including the CB thermal growths are validated by analytical and experimental data from the references. CB design objectives are set and then rotor drop simulations are conducted with major CB design parameters: friction coefficient at the rotor/inner race contact, axial preload, oil viscosity of SFD and one-axis side load from MBs. The numerical results are compared using 14 performance indices to identify improved CB design features.

2. Simulation models

2.1. Rotor drop simulation model

An energy storage flywheel with magnetic suspensions is shown in Fig. 1. The flywheel is attached to the rotor via a self-expandable and flexible hub ensuring low stress at extremely high
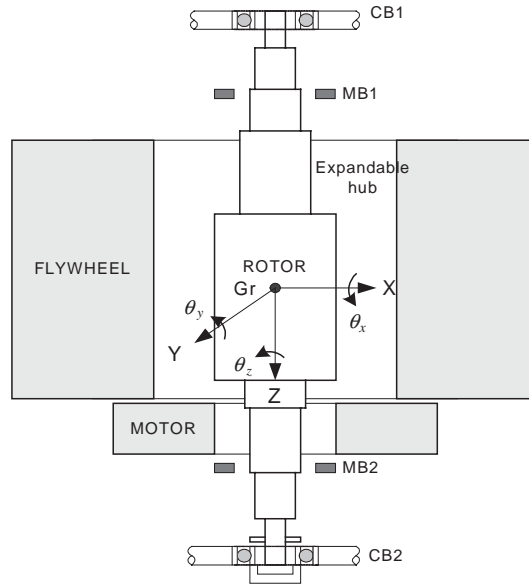
Fig. 1. Energy storage flywheel with magnetic suspensions.

speed. The hub and auxiliary supports (o-ring stiffness) are flexible elements compared to rigidity of the rotor. Fig. 1 does not capture proportions based on the actual dimensions of the flywheel and the rotor, but the actual ratio of rotor length to flywheel diameter is smaller than it appears in Fig. 1. Hence, the rigid rotor model is used here. The rigid flywheel, rotor and motor are modeled with 16 degrees of freedom (dof) including the cross-coupled hub stiffness and damping, and the gyroscopic moments. The equations of motion for the energy storage flywheel system are available in Appendix A. The rotor has three translational and rotational motions, while the flywheel and the motor have three translational and two rotational motions, each. The flywheel and the motor have unbalance masses with 90° phase difference from each other, and the rotor is assumed to be well balanced. The top CB is modeled as a 5 dof system as shown in Fig. 2. Each race has two translational dof in the radial direction, and in addition, the inner race has one rotational motion in the axial direction. The SFD in parallel to o-rings provides the viscous damping force to the CB, which has little inherent damping. The bottom CB is modeled as a 7 dof system including the axial transverse motions of the races. The CBs are modeled as back-to-back duplex pairs at each end. Duplex bearings are matched pairs of bearings with a built-in means of preloading to greatly increase radial and axial rigidity. They also have advantages such as easy assembly and minimum runout.

The frame of reference (O, X, Y) is fixed to the machinery frame as shown in Fig. 2. The geometric centers of the rotor and bearing inner race are O_r and O_b, respectively. (x, y) is the location of O_r in the reference frame, while (x_b, y_b) is the location of O_b. Normal (F_n) and tangential $(F_t,$ friction) contact forces are determined using the stiffness K_c representing the Hertzian contact force [13]. The bearing stiffness K_b as a function of inner race speed and axial preload is calculated using the iterative Newton–Raphson method [10]. The terms K_s and C_s
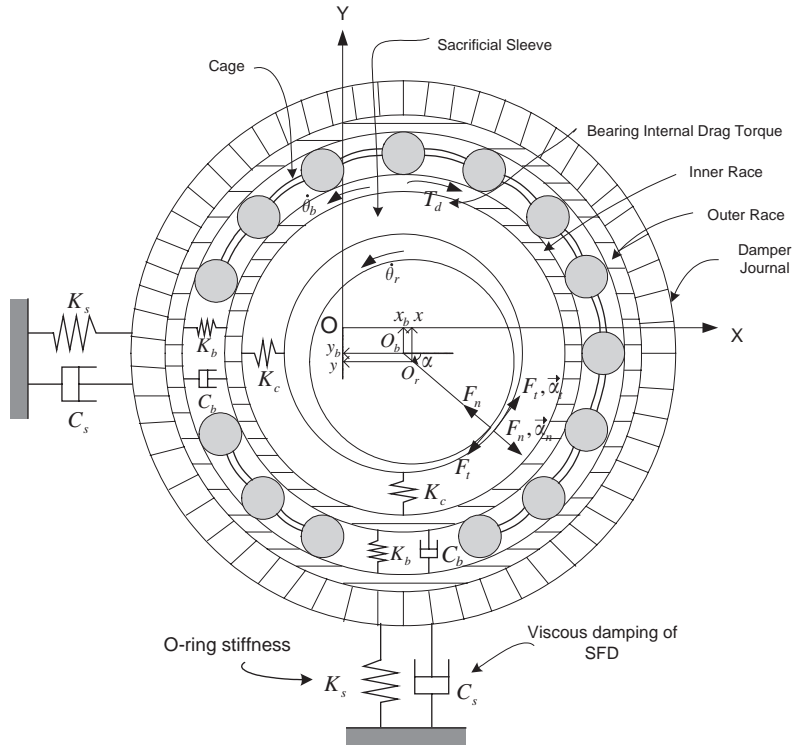
Fig. 2. Auxiliary support system including squeeze film damper.

represent the o-ring stiffness and FE SFD viscous damping force, respectively. The axial model of the integrated flywheel rotor and bottom CB is explained in Appendix A. The bottom CB is accelerated by the axial and radial contacts with the rotor, while the top CB only by the radial contact.

From Fig. 2, the angle at contact between rotor and CB is

$$\alpha_j = \tan^{-1}\left(\frac{y_j - y_{bj}}{x_j - x_{bj}}\right), \quad j = 1, 2, \tag{1}$$

where subscripts 1, 2 represent the top and bottom CBs, respectively.

When the rotor has a contact with the CB, a modified Hertzian [13] contact normal force F_n is applied as

$$F_{nj} = \begin{cases} K_c s_j^n (1.5\alpha \dot{s}_j + 1) & \text{if } s_j \geqslant 0, \\ 0 & \text{if } s_j < 0, \end{cases} \tag{2}$$

where $j = 1, 2$; $s_j = \sqrt{(x_j - x_{bj})^2 + (y_j - y_{bj})^2} - c$ and the contact stiffness K_c depends on material property and contact geometry. The constant c is the CB radial clearance, α has a value between 0.08 and 0.2 for steel, and n is dependent on the type of contact: here $n = 10/9$. The friction

force is then

$$F_{tj} = \mu_d F_{nj}, \quad j = 1, 2, \tag{3}$$

as long as slipping exists at the contact point, where μ_d is a dynamic friction coefficient.

When relative tangential velocity at the contact becomes zero, a rolling condition is applied and a detailed derivation of the rolling conditions is available in Ref. [10].

2.2. Detailed auxiliary bearing and damper models

Accurate prediction of the bearing stiffness is crucial in the rotor drop simulation because the bearing stiffness is significantly influenced by dimension, material, inner race speed and preload amount. The full procedure to obtain an accurate bearing stiffness and model verification is available in the author's previous works [10,14], and it can be summarized as follows.

Assuming the outer race is fixed, the load equilibrium equations of the inner race are

$$\{F\} + \sum_{j=1}^{n} T'_j \{Q\}_j = \{0\}, \tag{4}$$

where the external force vector $\{F\}$ is applied to the inner race with the displacement vector $\{X\}$, the vector $\{Q\}_j$ represents the Hertzian contact load applied to the jth ball, and n is the number of balls. The matrix T_j transforms the reference frame to the jth ball coordinate, i.e., $\{u\}_j = T_j\{X\}$. The jth ball load equilibrium equations including centrifugal force F_c are derived:

$$\begin{Bmatrix} F_r \\ F_z \end{Bmatrix} = \begin{Bmatrix} Q_i \cos\alpha_i - Q_e \cos\alpha_e + F_c \\ Q_i \sin\alpha_i - Q_e \sin\alpha_e \end{Bmatrix} = \begin{Bmatrix} 0 \\ 0 \end{Bmatrix}, \tag{5}$$

where $Q_{i,e}$ are the Hertzian contact loads, $\alpha_{i,e}$ are contact angles, and subscripts i, e represent the inner and the outer races.

Since Eqs. (4) and (5) are highly nonlinear, the unknown inner race displacement vector $\{X\}$ is solved for the linearized Eqs. (4) and (5) using the iterative Newton–Raphson method. After the convergence of solution, the bearing stiffness matrix is determined as

$$K_X = -\sum_{j=1}^{n} T'_j \cdot \left[\frac{\partial\{Q\}}{\partial\{u\}^T}\right]_j \cdot T_j. \tag{6}$$

The bearing stiffness is a diagonal element of the stiffness matrix K_X.

Assuming an incompressible Newtonian fluid, the Reynold's equation governs the characteristics of oil film between two cylinders neglecting sliding effects:

$$\nabla \cdot \left(\frac{\rho h^3}{12\mu} \nabla P\right) = \frac{\partial}{\partial t}(\rho h), \tag{7}$$

where ρ is the fluid density, h is the film thickness, μ is the viscosity, and P is the fluid pressure. The functional [15] corresponding to Eq. (7) is

$$J(P) = \int_A \left\{\frac{\rho h^3}{24\mu} \nabla P \cdot \nabla P + \frac{\partial}{\partial t}(\rho h)P\right\} dA. \tag{8}$$

Use interpolation functions and differentiate Eq. (8) with respect to the pressure P to minimize the functional $J(P)$. The FE model for oil film pressure vector $\{P^{(e)}\}$ is then derived as

$$\lfloor K^{(e)} \rfloor \cdot \{P^{(e)}\} = \{S^{(e)}\} + \{L^{(e)}\}. \tag{9}$$

The interpolation functions for a simple triangular element are used here.

Fig. 3 shows the geometry of a SFD with (x, y) as the coordinates of the SFD journal center O_j in the fixed reference frame (X, Y). The minimum film thickness is located at the point A, while the maximum film thickness at the point B. The angle θ is oriented from the X-axis, and the angle θ' from the maximum film thickness. Since the point B is not fixed in space, the frame $(\tilde{X}, \tilde{Y})$ follows the maximum film thickness. The film thickness h and squeeze velocity $\dot{h}$ are

$$h = c_{sf} - x\cos\theta - y\sin\theta, \quad \dot{h} = -\dot{x}\cos\theta - \dot{y}\sin\theta, \tag{10}$$

where c_{sf} is the nominal clearance of SFD.

Fig. 4 shows the FE mesh and boundary conditions on the SFD journal. The FE mesh reference frame $(\tilde{X}, \tilde{Y})$ has its origin B. Since the fluid flow is assumed to be symmetric about the mid-plane, only one-half of the axial length $L_j/2$ is utilized in the FE model. The mass flow rate across the mid-plane is set to zero, i.e., $\bar{q}_n = 0$ along the boundary $\tilde{Y} = L_j/2$, and the supply pressure P_a is specified along $\tilde{Y} = 0$. Since the film cavitation can occur as the journal eccentricity and whirling frequency increase, a back-substitution algorithm is applied to replace negative pressures with zeros for the cavitated regions ($P < 0$). Once the nodal pressures for an element are determined, the viscous damping forces in the radial and tangential directions are calculated from

$$\begin{Bmatrix} F_r \\ F_t \end{Bmatrix} = \frac{2}{3}\sum_{e=1}^{ne}(P_1^{(e)} + P_2^{(e)} + P_3^{(e)}) \cdot \begin{Bmatrix} \cos\left(\frac{\tilde{X}^{(e)}}{R_j}\right) \\ \sin\left(\frac{\tilde{X}^{(e)}}{R_j}\right) \end{Bmatrix} A^{(e)}, \tag{11}$$

where the parameter ne is the number of elements, and $A^{(e)}$ is the area of the eth element.
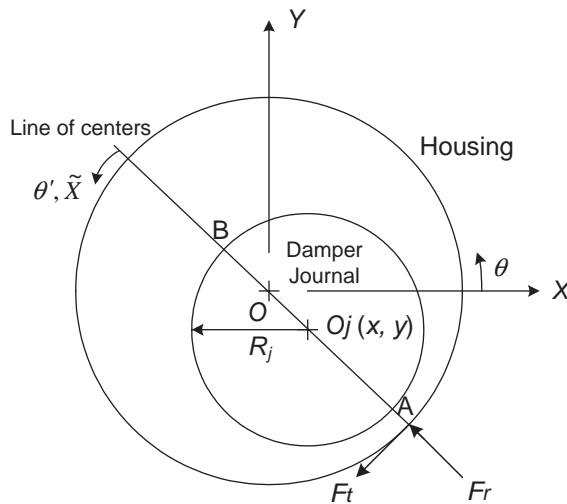

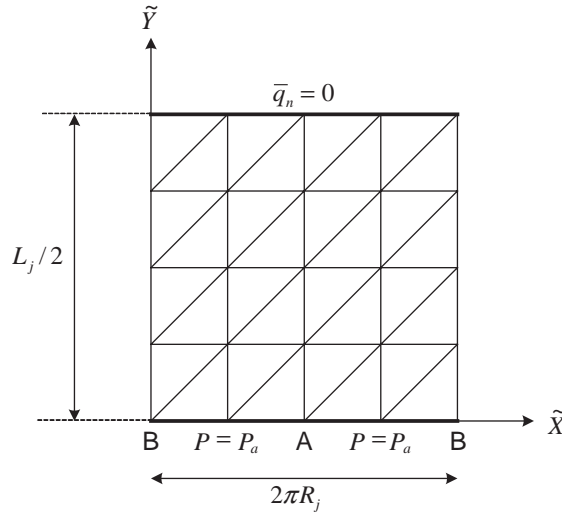Fig. 3. Squeeze film damper geometry.

Fig. 4. Boundary conditions of SFD model.

The power loss [14] due to viscous dissipation in the annular oil film is estimated as

$$H_{sf} = \frac{1}{6\mu} \sum_{e=1}^{ne} h_{(e)}^3 \cdot \left[\left(\frac{\partial P}{\partial \tilde{X}} \right)_{(e)}^2 + \left(\frac{\partial P}{\partial \tilde{Y}} \right)_{(e)}^2 \right] \cdot A^{(e)}. \tag{12}$$

An initial oil viscosity μ_i is updated according to the oil temperature increase ΔT, i.e., $\mu = \mu_i e^{-\beta \Delta T}$, where the viscosity coefficient β is always positive.

The analytical results from the FE SFD are compared with the test data from Ref. [16] collected for the offset circular whirl with respect to the reference frame center O. The comparisons of the viscous damping forces are made in Fig. 5 for the three meshes from the journal position $0°$ to $330°$ with $30°$ increment. Although the tangential force shows a noticeable difference above the journal position $150°$, the FE SFD results follow the experimental data with consistent trends, especially for the radial force.

2.3. Bearing thermal model

A ball bearing has a variety of heat sources, and here two major sources are considered during the rotor drop: rotor/CB mechanical rub and drag torque. The empirical formula for the drag torque due to external loads was derived by Palmgren [17] as

$$T_l = f_1 F_{ex} d_m, \tag{13}$$

where f_1 is a factor depending on bearing design and bearing load, and the force F_{ex} depends on the magnitude and direction of the external loads. The drag torque [17] due to lubricant and operating speed is obtained from

$$T_v = \begin{cases} 10^{-7} f_o (v_o n)^{2/3} d_m^3 & \text{for } v_o n > 2000, \\ 160 \cdot 10^{-7} f_o d_m^3 & \text{for } v_o n \leqslant 2000, \end{cases} \tag{14}$$
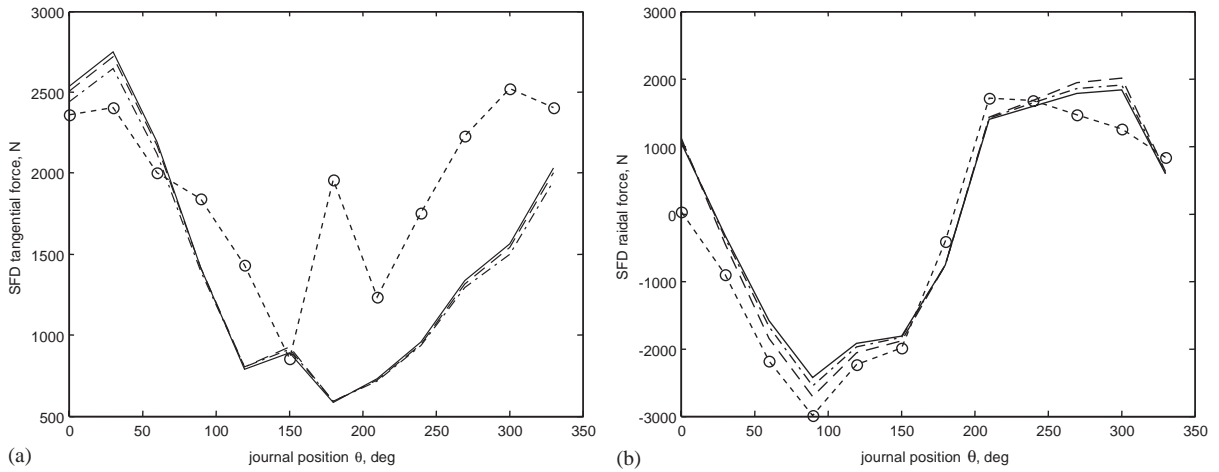
Fig. 5. Comparison of (a) tangential and (b) radial damper forces: ∘, test data [16]; solid, 128×40 FE SFD; dash-dot, 64×20 FE SFD; dash, 32×10 FE SFD.

where the parameter v_o is the kinematic viscosity of lubricant given in cST, n is the inner race speed in rev/min, and f_o is a factor depending on the bearing type and lubrication method. For the grease-packed ball bearings, the factor f_o ranges from 1.5 to 5. The total bearing drag torque is the sum of Eqs. (13) and (14), and the power loss $H_{i,e}$ is calculated by multiplying the total drag torque by the bearing operating speed in rad/s.

The power loss generated by the rotor/CB mechanical rub is derived from Fig. 2.

$$H_r = \vec{F}_t \cdot \vec{V}_{\text{rel}} = F_t(R_r \dot{\theta}_r - R_b \dot{\theta}_b) + F_t[(\dot{x}_b - \dot{x})\sin \alpha + (\dot{y} - \dot{y}_b)\cos \alpha], \tag{15}$$

where $\vec{V}_{\text{rel}}$ is the tangential relative velocity between the inner race and the rotor at the contact, and R_r, R_b denote the rotor radius and the inner race bore radius, respectively.

The total power loss of the rotor drop model is

$$H_{\text{total}} = \sum_{j=1}^{2} (H_{i,e}^j + H_r^j), \tag{16}$$

where superscripts 1, 2 indicate the top and the bottom CBs. The heat energy loss is then obtained by time integrating the power loss.

A CB thermal model is developed based on Jorgensen's work [12], which proposed a steady-state 1D bearing heat transfer model with an assumption that the heat flux passing a circle centered at the origin of bearing reference frame was uniform. The heat flux between two thermal nodes is described as their temperature difference divided by the thermal resistance, which is a function of geometry and thermal conductivity. The following assumptions are utilized in modeling: (a) the CB is composed of lumped heat mass elements, (b) the power loss due to the rotor/CB mechanical rub is applied equally to the rotor and the inner race, and (c) the conduction heat transfer passes through the SFD. The temperature nodes in the cross-sectioned ball bearing combined with SFD are shown in Fig. 6. The length L_s refers to the distance from the axial center
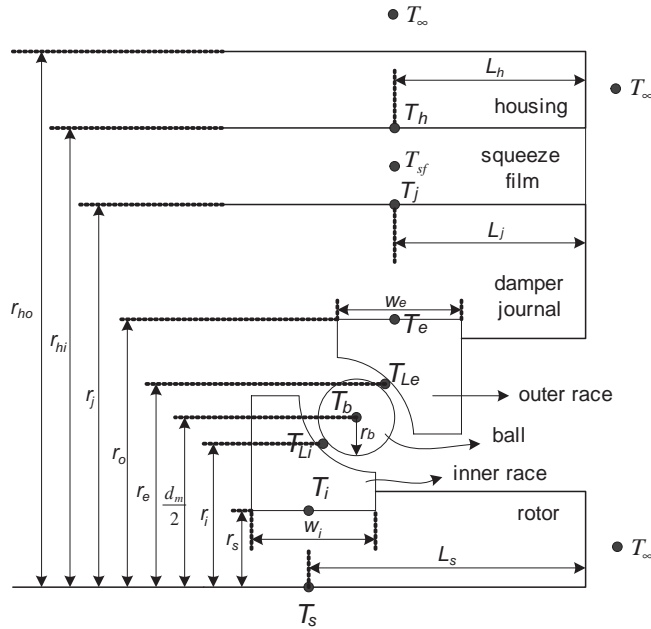
Fig. 6. Cross-sectioned bearing with thermal nodes.

of the inner race to one end of the rotor, and the lengths L_j, L_h denote the axial lengths of the SFD journal and the housing, respectively. The widths w_i, w_e of the inner and outer races are assumed to be the same. Fig. 7 is the heat transfer network for Fig. 6, which consists of the thermal resistances, heat sources, and heat masses. As long as the rotor has contacts with the CB, the temperature nodes T_i and T_s are connected. Otherwise, their connection is lost, and the power loss H_r is equal to zero. The thermal resistances are listed in Table 1. A free convection coefficient h [17] is approximated as a function of the temperature difference, $h = 23(T - T_\infty)^{0.25}[\text{W/m}^2\,^\circ\text{C}]$, and is used at the housing and rotor axial surfaces.

The first-order thermal equation for each temperature node is derived as

$$mC_p\mathrm{d}T/\mathrm{d}t = Q_i - Q_o, \tag{17}$$

where the parameter m is a lumped heat mass, C_p is the specific heat, and $Q_{i,o}$ are the heat flux in and out.

With a linear temperature distribution in the radial direction, the thermal expansion ε_e [18] of the outer race jointed with the SFD journal is

$$\varepsilon_e = \frac{\xi_e}{3}\frac{(1+v_e)r_e}{r_e+r_j}[\Delta T_{Le}(2r_e+r_j) + \Delta T_j(2r_j+r_e)], \tag{18}$$

where ξ_e [m/m $^\circ$C] is the thermal expansion coefficient of the outer race, v_e is the Poisson's ratio, and ΔT indicates the thermal growth from an initial temperature. Similarly, the thermal expansion for the inner race is described as

$$\varepsilon_i = \frac{\xi_i}{3}\frac{(1+v_i)r_s}{r_i+r_s}[\Delta T_i(2r_s+r_i) + \Delta T_{Li}(2r_i+r_s)]. \tag{19}$$
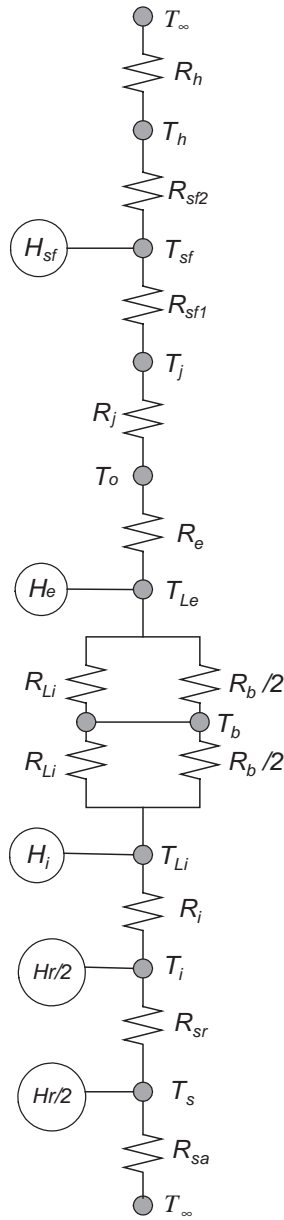
Fig. 7. Heat transfer network of catcher bearing.

The thermal expansion of a ball is

$$\varepsilon_b = \xi_b r_b \Delta T_b, \tag{20}$$

where r_b is the ball radius.

The thermally induced contact load due to the relative thermal expansion ε is predicted by

$$F_t = k\varepsilon^{1.5}, \tag{21}$$

Table 1
Thermal resistances of heat transfer network

Ball/lubricant	Inner race/shaft	Outer race/journal
$R_{Li} \approx \dfrac{r_b}{k_l(2\pi r_i w_i - \pi n r_b^2)}$	$R_i = \dfrac{\ln(r_i/r_s)}{2\pi k_i w_i}$	$R_e = \dfrac{\ln(r_o/r_e)}{2\pi k_e w_e}$
$R_{Le} \approx \dfrac{r_b}{k_l(2\pi r_e w_e - \pi n r_b^2)}$	$R_{sr} = \dfrac{1}{\pi k_s w_i}$	$R_j = \dfrac{\ln(r_j/r_o)}{2\pi k_j w_e}$
$R_b \approx \dfrac{1}{n k_b \pi r_b}$	$R_{sa} = \dfrac{L_s}{k_s \pi r_s^2} + \dfrac{1}{h_s \pi r_s^2}$	
SFD	**Housing**	
$R_{sf1} = \dfrac{\ln((r_j + c_{sf}/2)/r_j)}{2\pi k_{sf} L_j}$	$R_{hr} = \dfrac{\ln(r_h/r_o)}{2\pi k_h L_h} + \dfrac{1}{h_h 2\pi r_h L_h}$	$R_h = \dfrac{R_{hr} R_{ha}}{R_{hr} + R_{ha}}$
$R_{sf2} = \dfrac{\ln(r_{hi}/(r_j + c_{sf}/2))}{2\pi k_{sf} L_j}$	$R_{ha} = \dfrac{L_h}{2\pi k_h (r_h^2 - r_o^2)} + \dfrac{1}{\pi h_h (r_h^2 - r_o^2)}$	

where $\varepsilon = \varepsilon_b + 0.5(\varepsilon_i - \varepsilon_e)\cos\alpha$, α is the bearing contact angle, and k is the Hertzian contact stiffness. Stein and Tu [19] modified Palmgren's formula, Eq. (13), including the effect of the thermally induced load

$$T_l = f_1(E_{ex} + F_t)d_m. \tag{22}$$

The 1D bearing thermal model is validated using the test data from Ref. [20], thermal growths on outer races of two types of ball bearings: steel and ceramic balls. The ball bearings in the spindle 1 were arranged as a back-to-back duplex pair with $40°$ contact angle and grease-packed lubrication, and those in the spindle 2 as a quadriplex set with $17°$ contact angle and oil-air lubrication. Axial preloads were set at 1500 and at 75 N. The steady-state temperatures were measured using thermocouples attached to the outside surfaces of the outer races. Fig. 8 shows the comparison of the numerical and experimental results for the thermal growths of the steel and ceramic ball bearings versus the operating speed. It is noticeable in the spindle 1 that there is no significant difference between the steel and ceramic bearings below 3000 rev/min and that the temperature of the steel bearing increases drastically from 3000 rev/min. In the spindle 2, there is no considerable difference below 10,000 rev/min and then, the steel bearings show a large temperature rise above 10,000 rev/min. The numerical prediction from the bearing thermal model shows consistent trends with the test data.

3. Simulation results and discussion

A variety of rotor drop simulations were conducted to illustrate implementation of the model capabilities. The dimension and material characteristics of the CB and SFD are listed in Table 2, while the specifications for the rotor, flywheel and motor in Table 3. When a simulation starts, the flywheel rotor spinning at 40 000 rev/min is axially dropped onto the bottom CB by
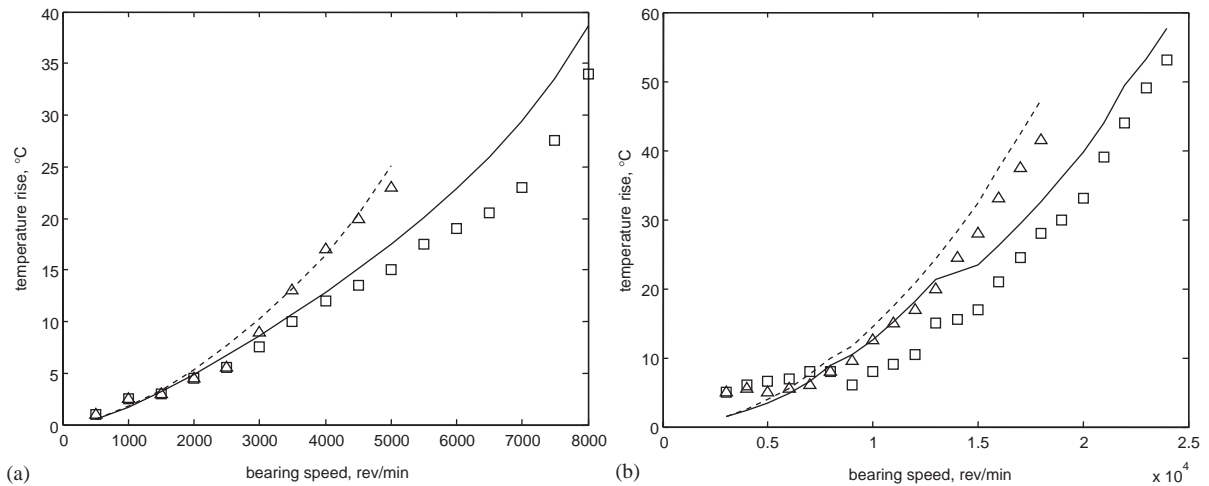
Fig. 8. Thermal growths of outer ring (a) in spindle 1 and (b) in spindle 2: solid, ceramic, numerical; $\square$, ceramic, test [20]; dotted, steel, numerical; $\triangle$, steel, test [20].

Table 2
Specifications of CB and SFD

Dimension and property	Specification
Geometric specification	
Bore diameter	1.7 (cm)
Outside diameter	3.5 (cm)
Width	1.0 (cm)
Number of balls	16
Initial contact angle	15°
Axial preload, F_a	88.96 (N)
Number of rows	2, DB duplex pair
Material specification	
Density of ball: ceramic	3.2 (g/cm^3)
Density of races: steel	7.8 (g/cm^3)
Elastic modulus of ball	315 (GPa)
Poisson's ratio of ball	0.26
Elastic modulus of races	208 (GPa)
Poisson's ratio of races	0.3
SFD specification	
O-ring stiffness, K_s	3.5E+6 (N/m)
Axial length of journal	2.5 (cm)
Radius of journal	5 (cm)
Radial clearance	0.127 (mm)
Supply oil pressure	0.2 (MPa)
Viscosity of oil	See Table 4

Table 3
Specifications of energy storage flywheel system

Dimension	Specifications
Rotor	
Mass	2.39 kg
Transverse MOI	0.0087 kg m^2
Polar MOI	0.0011 kg m^2
Radial clearance of CBs	0.254 mm
Radial clearance of MBs	0.508 mm
Axial clearance	0.381 mm
Side loads from MBs, F_{sl}	444.82 N
Friction coeff., $\mu_{s,d}$	See Table 4
Flywheel	
Mass	26.71 kg
Polar MOI	0.7237 kg m^2
Transverse MOI	0.4460 kg m^2
Unbalance eccentricity	0.00254 mm
Motor	
Mass	2.65 kg
Polar MOI	0.0060 kg m^2
Transverse MOI	0.0033 kg m^2
Unbalance eccentricity	0.00254 mm
Total	
Polar MOI	0.7308 kg m^2
Initial spinning speed	40,000 rev/min

gravity and simultaneously moves toward the CBs with an initial velocity from the reference frame center.

The non-dimensional CB stiffness depending on the speed and axial preload is presented in Fig. 9, which is based on the radial stiffness 2.0885E + 5 N/mm for zero speed and 89 N preload. At the zero speed, the radial stiffness for the preload 356 N increases 50% from that for 89 N, while the axial stiffness for 356 N increases 20% from that for 89 N. The radial stiffness at 40,000 rev/min decreases 20% from that at 0 rev/min for the preload 89 N, while the axial stiffness decreases only less than 5%.

Numerical solutions are obtained using the fourth-order Runge–Kutta integration algorithm with a variable time step. The total integration time is 0.5 s and the display time step is 4×10^{-5} s. To treat contact status, calculate the relative distance, s between the rotor and inner race geometric centers. If s is greater than the nominal CB clearance 0.254 mm, the normal and tangential contact forces are calculated and applied to the rotor and the inner race. If s is less than the clearance, the contact forces become zero. Rolling occurs theoretically when the relative tangential velocity at the contact is exactly zero, but this may not happen numerically. Thus, a very small boundary (1E−8) is added around the zero relative velocity, and if the velocity is within this boundary, the rolling condition is applied to determine the tangential contact force and if the velocity exceeds this boundary, the slipping condition is reapplied.
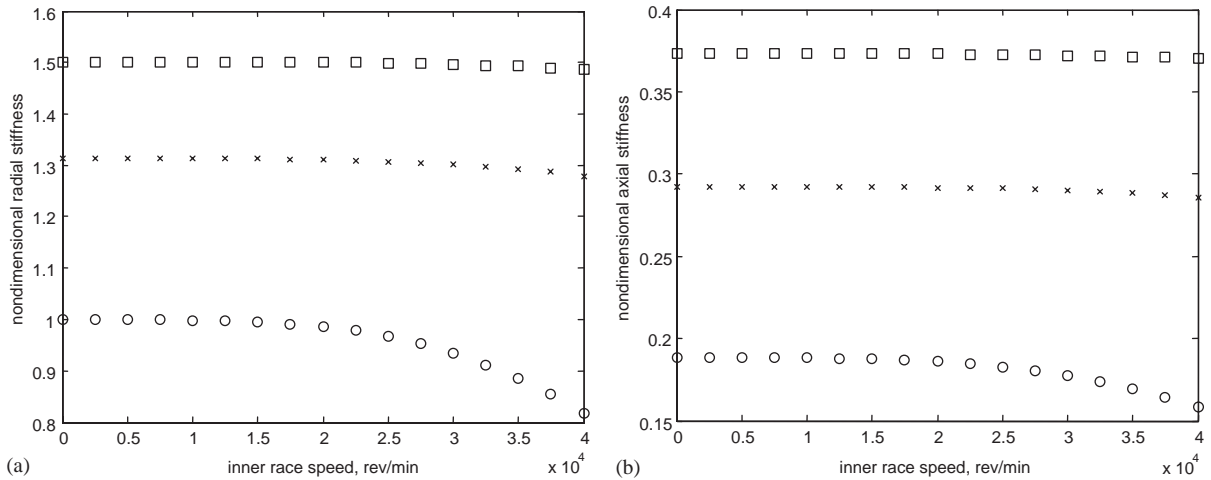
Fig. 9. Non-dimensional CB stiffness versus inner race speed and preload ($\circ$, 89 N; $\times$, 222 N; $\square$, 356 N): (a) radial stiffness, (b) axial stiffness, base stiffness $= 2.0885E + 5\,\text{N/mm}$.

To increase computation efficiency, the matrix $[K]$ in the FE SFD model, Eq. (9), is updated only when the distance between the damper journal centers at the present time step and at the last update time is greater than 5% of the SFD radial clearance. It is observed from the simulations that the SFD does not function as a damper at a high eccentricity ratio because of the high nonlinearity and large cavitated area on the journal. Furthermore, the high eccentricity ratio over 0.9 is usually observed when a high-speed backward whirl is engaged. Hence, if the eccentricity ratio is greater than 0.9, the SFD is turned off, and a contact force is generated when the ratio is beyond 1. The FE SFD model employs a mesh of 10 equal divisions axially and 32 equal divisions circumferentially, which results in 640 triangular elements in the full journal mesh. The initial temperature of the CB components and the ambient temperature are set at 27 °C.

To investigate the effects of CB design on rotor behavior and thermal growth, the parametric studies are performed for the major CB design parameters: the friction coefficient of the rotor/inner race interface ($\mu_{s,d}$), the axial preload (F_a), the oil viscosity in the SFD (μ_o), and X-axis side loads from the MBs (F_{sl}). The last parameter may be useful in the event that MB control is lost while the MB actuator remains operative. Table 4 shows the simulation cases.

The following performance indices (PIs) are utilized to compare and characterize the simulation responses: (1) peak normal contact force (N); (2) peak impulse due to normal contact force (N s); (3) minimum air gap at MBs (mm); (4) final rotor whirl rate (rev/min); (5) maximum power loss due to drag torque (W); (6) maximum power loss due to mechanical rub (W); (7) maximum total power loss (W); (8) maximum heat energy due to drag torque (J); (9) maximum heat energy due to mechanical rub (J); (10) maximum total heat energy (J); (11) thermal growth ΔT_i (refer to Fig. 6) (°C); (12) thermal growth ΔT_{Li} (°C); (13) thermal growth ΔT_b (°C); (14) thermal growth ΔT_{Le} (°C).

The first PI indicates the maximum contact normal force on the CBs, and the second PI, the time integration of the first PI, refers to the duration of the contact normal force. The minimum air gap at the MBs means how much radial air gap is available at the MBs (how safe MB stators

Table 4
Simulation cases

Simulation no.	μ_s, μ_d	F_a (N)	SFD viscosity (cP) at 40 °C	F_{sl} (N)
Case I: fiction coefficient effects				
I-1	0.3, 0.1	88.96	30.5	0
I-2	0.35, 0.15	88.96	30.5	0
I-3	0.4, 0.2	88.96	30.5	0
I-4	0.45, 0.25	88.96	30.5	0
I-5	0.5, 0.3	88.96	30.5	0
Case II: axial preload effects				
II-1	0.4, 0.2	88.96	95.7	444.82
II-2	0.4, 0.2	222.41	95.7	444.82
II-3	0.4, 0.2	355.86	95.7	444.82
Case III: damper oil viscosity effects				
III-1	0.4, 0.2	88.96	8.7	0
III-2	0.4, 0.2	88.96	17.4	0
III-3	0.4, 0.2	88.96	30.5	0
III-4	0.4, 0.2	88.96	60.0	0
III-5	0.4, 0.2	88.96	95.7	0
III-6	0.4, 0.2	88.96	132.2	0
III-7	0.4, 0.2	88.96	194.9	0
Case IV: side load effects				
IV-1	0.3, 0.1	88.96	30.5	444.82
IV-2	0.35, 0.15	88.96	30.5	444.82
IV-3	0.4, 0.2	88.96	30.5	444.82
IV-4	0.45, 0.25	88.96	30.5	444.82
IV-5	0.5, 0.3	88.96	30.5	444.82

are), which is equal to 0.508 [mm] minus the maximum radial motion of the rotor at the MBs. The final rotor whirl rate at the bottom CB is monitored as the fourth PI. The fifth to seventh indices denote the maximum power loss due to the bearing drag torque and the rotor/CB mechanical rub, and the eighth to tenth the corresponding maximum heat energy loss. The 11th to 14th indices show the thermal growths ΔT of the bottom CB from the initial temperature. The CB design objectives here are to maximize the minimum air gap at the MBs, to minimize the contact normal force and impulse, and to minimize the CB thermal growths, while preventing the high-speed backward whirl.

Fig. 10 shows the orbital motions of rotor at the bottom CB for Case I. As the friction coefficient increases, the whirl amplitude of rotor and the radial thickness of the orbit band also increase. Note that the first-bounce direction becomes closer to the tangential direction to the contact point because the friction force has increased. The two groups of orbit bands are observed in the last case. Since the SFD is the only damping source in the auxiliary support system, when it fails, the high-speed backward whirl is fully developed and then the rotor hits the MB stators under the high dynamic loading as shown in the last case. When the one-axis side loads from the
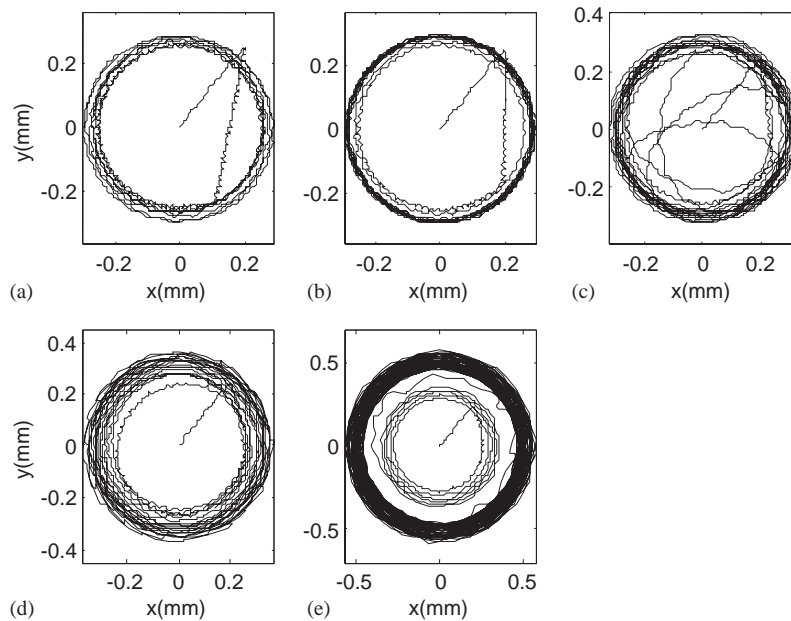
Fig. 10. Rotor orbit plots at CBs versus μ_d for Case I: (a) $\mu_d = 0.1$; (b) $\mu_d = 0.15$; (c) $\mu_d = 0.2$; (d) $\mu_d = 0.25$; (e) $\mu_d = 0.3$; MB clearance 0.508 mm.

MBs are applied, the orbital motions are dramatically stabilized for all the coefficients of friction as shown in Fig. 11. The dotted circle is the CB clearance 0.254 mm. It is noticed in the orbit plot that the sliding arc length of rotor increases as the coefficient of friction increases.

Table 5 lists the PI values for Case I. The results for the PIs 4, 11–14 are for the end of the simulation time. The peak normal contact force and impulse enormously increase between Case I-4 and Case I-5 because of the dynamic loading caused by the high-speed backward whirl. The same trends apply to the power loss due to the rotor/CB mechanical rub. The minimum air gap significantly decreases between these cases and the minus sign in the last case indicates that the rotor has contacts with the MB stator. The CB thermal growths also increase as the friction coefficient increases, and the first case shows the lowest growths. The PI values that fulfill the CB design objectives are checked. Table 6 shows the PI values for Case IV. The normal contact force, impulse and minimum air gap do not vary much in accord with the friction coefficient change. The power loss shows about 5000 W increment between the neighboring cases, while the heat energy loss about 150–250 J increment.

Figs. 12 and 13 compare the PI values for Cases I, IV based on the CB design objectives to examine the effect of the MB side loads on the rotor drop dynamics and thermal growth. The results of Case I-3 are used for calculating the non-dimensional PI values in Fig. 12. The peak normal forces in Case I are about 600 N lower than those in Case IV between the friction coefficients 0.1 and 0.2, while the minimum air gaps in Case I are about 0.03 mm more than those in Case IV. However, the normal force and impulse at the coefficient 0.3 in Case I increase by a factor of more than 20, and the minimum air gap decreases below zero, while those in Case IV
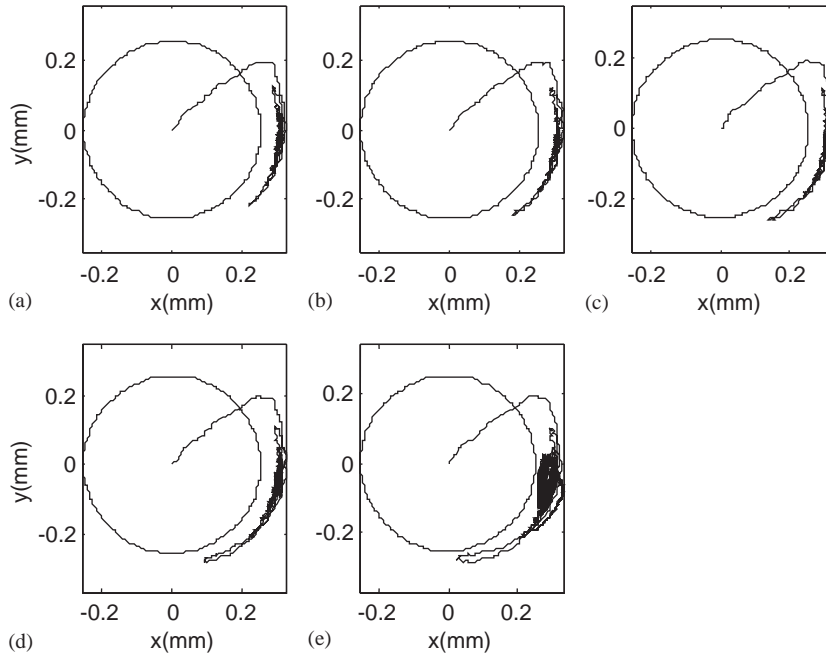
Fig. 11. Rotor orbit plots at CBs versus μ_d for Case IV: (a) $\mu_d = 0.1$; (b) $\mu_d = 0.15$; (c) $\mu_d = 0.2$; (d) $\mu_d = 0.25$; (e) $\mu_d = 0.3$; dotted circle is CB clearance 0.254 mm.

Table 5
Performance indices for Case I

PI #	I-1	I-2	I-3	I-4	I-5
1	866.7 N ✔	868	997.9	4296.4	19393
2	33.8 N s ✔	90.1	160.8	270.1	4811.3
3	0.1904 mm ✔	0.1904	0.1837	0.1248	−0.1092
4	−1242 rev/min	−2524	−1365	−848.6	−8469
5	75.6 W	151.1	346.2	753.9	876
6	5875.4 W	8494	11,334	16,494	60,260
7	5875.6 W	8494	11,334	16,677	60,728
8	14.1 J	26.8	65.8	203.2	254.4
9	862.7 J	1357	1964.4	2163.7	2117.6
10	876.8 J	1383.7	2032.2	2366.9	2372
11	38.6 °C ✔	47.8	55.6	69.4	78.4
12	21.0 °C ✔	27.5	37.9	49.9	52.8
13	12.3 °C ✔	17.7	29.3	48.8	52.8
14	3.4 °C ✔	5.1	9.3	20.1	24.4

barely change. The thermal growths for the coefficients 0.1, 0.15 in Case I are lower than those in Case IV, however the thermal growths in Case I become higher than those in Case IV from the coefficient 0.2 and the difference is greater as the coefficient increases. It is summarized from

Table 6
Performance indices for Case IV

| PI #	IV-1	IV-2	IV-3	IV-4	IV-5
1	1508.7 N	1527.8	1546.6	1566.6	1547.8
2	122.2 N s	121.4	120.3	118.4	114.3
3	0.1603 mm	0.1607	0.1611	0.1616	0.1625
4	420 rev/min	394	358	1180	0.3
5	125.4 W	172.3	224.6	281.3	347.1
6	10051 W	15,219	20,546	25,975	30,574
7	10051 W	15,220	20,546	25,975	30,575
8	26.7 J	36.9	48.5	61	74.8
9	1276.7 J	1518.9	1723.2	1888.7	2022.9
10	1303.4 J	1555.8	1771.6	1949.7	2097.8
11	44.3 °C	48.2	51.2	53.5	55.5
12	26.6 °C	30.0	33.0	35.8	38.6
13	17.2 °C	20.4	23.3	26.7	30.2
14	5.2 °C	6.4	7.6	8.8	10.2
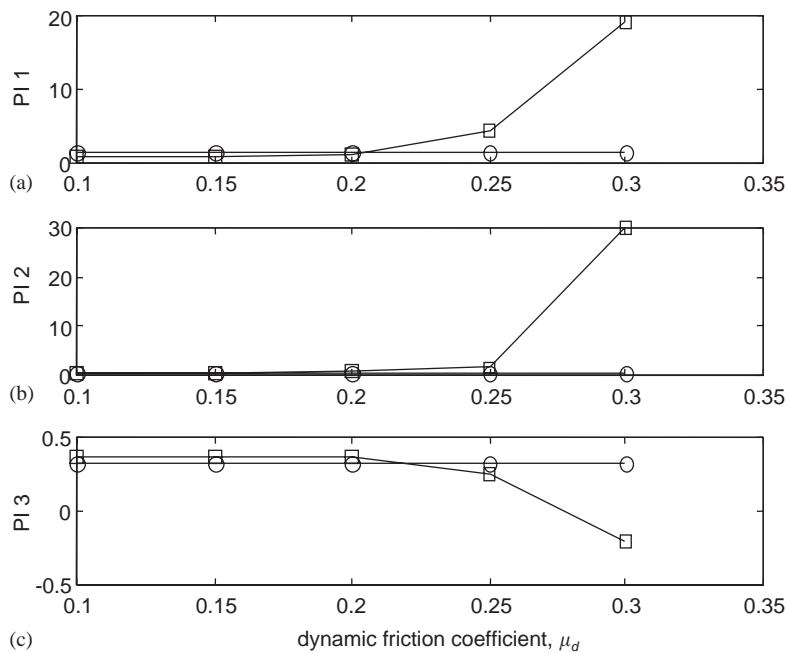
Fig. 12. Non-dimensional (a) PI 1, (b) PI 2 and (c) PI 3 versus μ_d: $\bigcirc$, Case IV; $\square$, Case I; base force = 997.9 N; base impulse = 160.8 N s; base MB air gap = 0.508 mm.

Cases I, IV that the MB side loads prevent the high-speed backward whirl and significantly reduce the thermal growths at the high friction coefficients although they increase the normal force, impulse and thermal growths at the low friction coefficients.
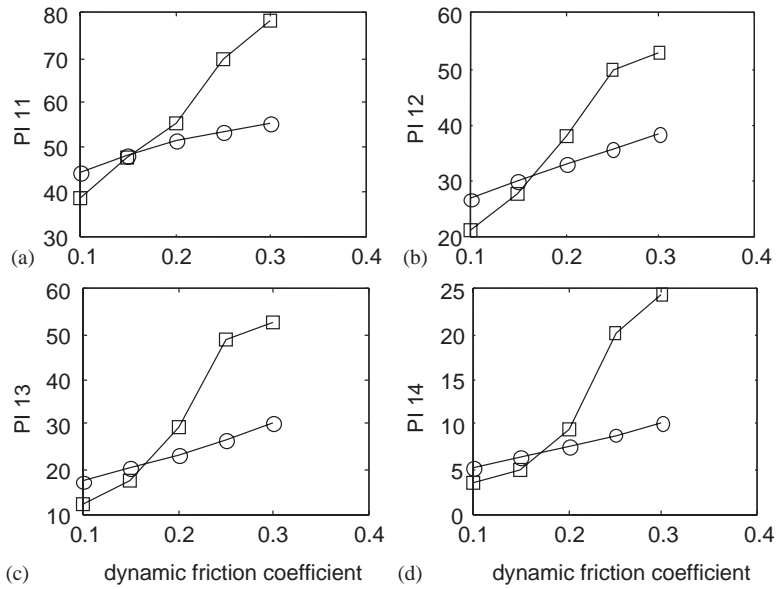
Fig. 13. Thermal growths (a) PI 11, (b) PI 12, (c) PI 13 and (d) PI 14 versus μ_d: ○, Case IV; □, Case I.

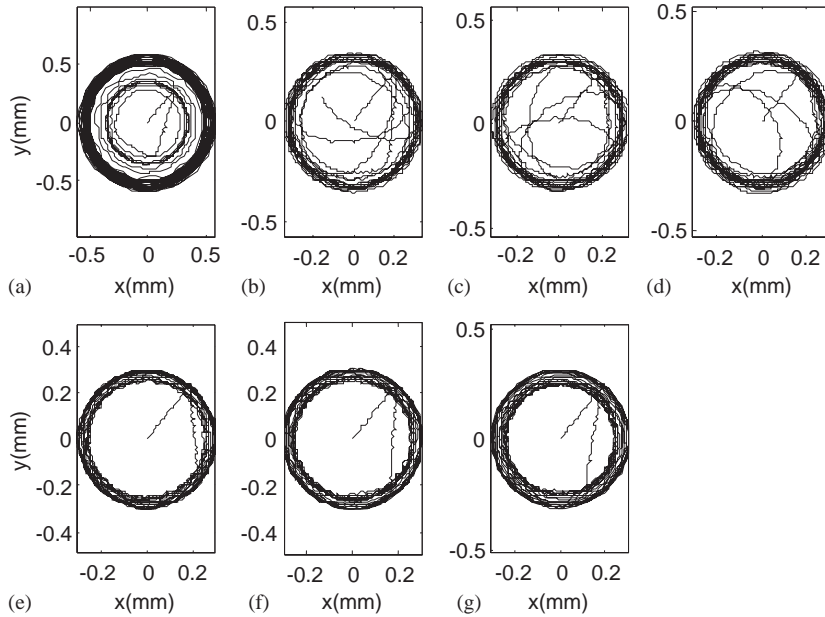

Fig. 14. Rotor orbit plots at CBs versus oil viscosity for Case III: (a) $\mu_o = 8.7$ (cP); (b) $\mu_o = 17.4$; (c) $\mu_o = 30.5$; (d) $\mu_o = 60$; (e) $\mu_o = 95.7$; (f) $\mu_o = 132.2$; (g) $\mu_o = 194.9$; MB clearance 0.508 mm.

Fig. 14 shows the orbital motions of rotor for Case III. The two groups of orbit bands are also observed in the first case, and the orbital motion with the 10 K rev/min backward whirl reaches the MB clearance 0.508 mm because of the insufficient damping. In the second to fifth cases, the

Table 7
Performance indices for Case III

PI #	III-1	III-2	III-3	III-4	III-5	III-6	III-7
1	20305 N	1133	997.9 ✔	1437.7	1586.6	2489.6	3625.7
2	4007.8 N s	189	160.8 ✔	237.2	304.3	347.5	387.7
3	−0.1235 mm	0.1650	0.1837	0.1905	0.2039 ✔	0.1966	0.1860
4	−10054 rev/min	−2320	−1365	−1397	−1404	−2072	−1064
5	837.8 W	416.7	346.2	531.2	613.2	675.4	752.9
6	49773 W	9084	11,334	14,444	17,332	19,693	28,269
7	50158 W	9084	11,334	14,444	17,332	19,799	28,385
8	186.3 J	76	65.8	105.8	162.2	204.8	238.8
9	2168.5 J	2074.3	1964.4	2170.7	2202.1	2167.2	2128.9
10	2354.8 J	2150.2	2032.2	2276.5	2364.3	2371.9	2367.7
11	72.6 °C	56.2	55.6 ✔	59.7	64.6	68.6	73.0
12	48.3 °C	39.7	37.9 ✔	43.5	48.0	50.3	52.1
13	46.3 °C	31.9	29.3 ✔	38.5	45.7	49.3	52.1
14	18.0 °C	10.3	9.3 ✔	13.0	17.6	20.7	23.4

whirl amplitude decreases as the oil viscosity increases. However, it increases again from the sixth case because an excessive damping locks up the support system.

Table 7 lists the PI values for Case III. The normal contact force and impulse in the first case increase more than 20,000 N and 4000 N s, respectively due to the high-speed backward whirl, and the minimum air gap decreases below zero. The power loss and the resulting thermal growths increase considerably compared to the next case. The PI values that fulfill the CB design objectives are checked. Figs. 15 and 16 show the PI values for Case III based on the CB design objectives. The results of Case III-3 are used for calculating the non-dimensional PI values in Fig. 15, and the PIs in the first case are omitted to make visible the difference between the other cases. The contact force and impulse have the minimum values at Case III-3, while the minimum air gap has the maximum value at Case III-5. The CB thermal growth at Case III-3 has the minimum value at each node as shown in Fig. 16. It is summarized from Case III that the SFD oil viscosity $\mu_o = 30.5$ cP (SAE 10) satisfies best the CB design objectives even though the viscosity $\mu_o = 95.7$ cP (SAE 30) provides the maximum air gap at the MBs 0.02 mm more than viscosity $\mu_o = 30.5$ cP.

Table 8 lists the PI values for Case II. Since the simulation time is short, the preload effects are not apparent here except for the increase of the power loss.

4. Conclusions

This paper presents detailed auxiliary bearing and damper models including CB thermal growths and applies those to a high-speed flywheel rotor drop on CBs to study the effects of CB design parameters on a rotor drop and the resulting thermal growths. Rotor drop simulations are conducted with the major CB design parameters, and the simulation results are then compared using a set of performance indices to identify improved CB design features and to find the parameters that satisfy the design objectives.
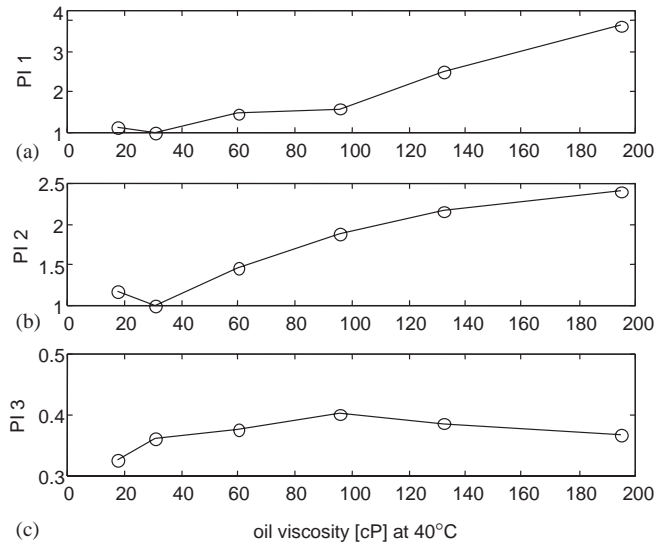
Fig. 15. Non-dimensional (a) PI 1, (b) PI 2 and (c) PI 3 for Case III, versus oil viscosity: base force = 997.9 N; base impulse = 160.8 N s; base MB air gap = 0.508 mm.
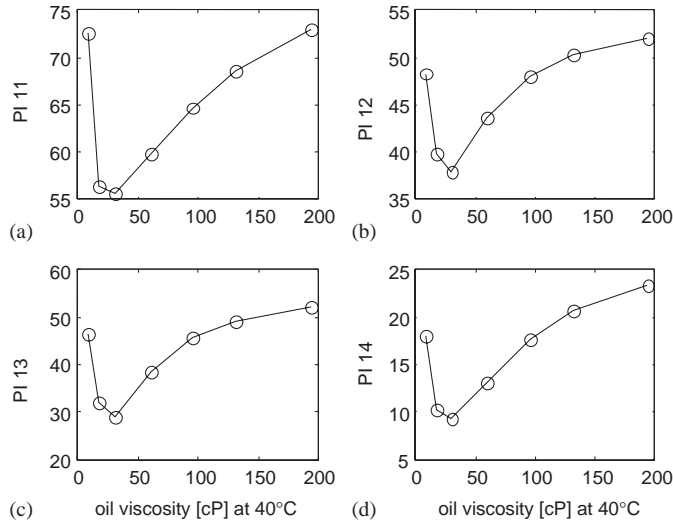

Fig. 16. Thermal growths (a) PI 11, (b) PI 12, (c) PI 13 and (d) PI 14 for Case III versus oil viscosity.

Based on the numerical analysis using the detailed bearing and damper models with thermal growths, CB design guides are suggested as follows:

- As shown in the simulations of Case I, the rotor drop dynamics and thermal growths drastically change between the friction coefficients $\mu_d = 0.25, 0.3$. Hence, it is an important step to find a

Table 8
Performance indices for Case II

PI #	II-1	II-2	II-3
1	997.9 N	990.2	1042.4
2	160.8 N s	159.3	158.9
3	0.1837 mm	0.1859	0.1863
4	−1365 rev/min	−2258	−2116
5	346.2 W	349	354.8
6	11334 W	11,495	11,732
7	11334 W	11,495	11,732
8	65.8 J	67	68.8
9	1964.4 J	1961.3	1966.9
10	2032.2 J	2028.4	2035.7
11	55.5 °C	56.3	56.6
12	37.8 °C	38.0	38.3
13	28.8 °C	29.1	29.5
14	9.2 °C	9.3	9.5

threshold friction coefficient above which a given rotor drop system enters into a high-speed backward whirl. Since reducing the friction coefficient is so critical to the stability of the rotor drop dynamics, surface finish and power/solid lubricants can be utilized on the rotor/CBs contact area.

- When the MBs remain operative, applying one-direction side loads help avoid a high-speed backward whirl. Although the side loads result in more normal contact force, more impulse, less minimum air gap and more thermal growths under the low friction coefficients, they prevent the rotor from entering a high-speed whirl under the high friction coefficients satisfying the CB design objectives.
- An optimum damping is found via the simulations of Case III, which satisfies best the CB design objectives. A lower damping than the optimum amount may induce a high-speed backward whirl, and a higher damping may increase the contact normal force, impulse and thermal growths.

Although the simulation model presented here is significantly improved from its counterparts in previous CB papers, it will be enhanced to include a 3D bearing model with individual ball and race motions, ball stress calculation and furthermore, CB life prediction in my planned future work. In addition, the numerical results will be benchmarked against experimental results from a CB test rig at NASA Glenn.

Acknowledgements

Appendix A. Equations of motion for the energy storage flywheel model

The equations of motion (e.o.m.) for the rigid motor with four dof are

$$M_m \ddot{x}_m = -K_{mtxx}(x_m - x_r - d_1\theta_{ry}) - C_{mtx}(\dot{x}_m - \dot{x}_r - d_1\dot{\theta}_{ry})$$
$$- K_{mtxy}(y_m - y_r + d_1\theta_{rx}) + M_m e_m \omega_z^2 \cos(\omega_z t),$$

$$M_m \ddot{y}_m = -K_{mtyy}(y_m - y_r + d_1\theta_{rx}) - C_{mty}(\dot{y}_m - \dot{y}_r + d_1\dot{\theta}_{rx})$$
$$- K_{mtyx}(x_m - x_r - d_1\theta_{ry}) + M_m e_m \omega_z^2 \sin(\omega_z t),$$

$$I_{mt}\ddot{\theta}_{mx} = -I_{mp}\omega_z\dot{\theta}_{my} - K_{mrxx}(\theta_{mx} - \theta_{rx}) - C_{mrx}(\dot{\theta}_{mx} - \dot{\theta}_{rx}) - K_{mrxy}(\theta_{my} - \theta_{ry}),$$

$$I_{mt}\ddot{\theta}_{my} = I_{mp}\omega_z\dot{\theta}_{mx} - K_{mryy}(\theta_{my} - \theta_{ry}) - C_{mry}(\dot{\theta}_{my} - \dot{\theta}_{ry}) - K_{mryx}(\theta_{mx} - \theta_{rx}),$$

where K_{mtxx} and K_{mtyy} are transverse stiffnesses of the expandable hub, C_{mtx} and C_{mty} are transverse dampings, K_{mtxy} and K_{mtyx} are transverse cross-coupled stiffnesses, K_{mrxy} and K_{mryx} are rotational cross-coupled stiffnesses, and d_1 is the distance between the motor and rotor mass centers with respect to the reference frame.

Similarly, the e.o.m. of the rigid flywheel are described as

$$M_f \ddot{x}_f = -K_{ftxx}(x_f - x_r - d_2\theta_{ry}) - C_{ftx}(\dot{x}_f - \dot{x}_r - d_2\dot{\theta}_{ry})$$
$$- K_{ftxy}(y_f - y_r + d_2\theta_{rx}) - M_f e_f \omega_z^2 \sin(\omega_z t),$$

$$M_f \ddot{y}_f = -K_{ftyy}(y_f - y_r + d_2\theta_{rx}) - C_{fty}(\dot{y}_f - \dot{y}_r + d_2\dot{\theta}_{rx})$$
$$- K_{ftyx}(x_f - x_r - d_2\theta_{ry}) + M_f e_f \omega_z^2 \cos(\omega_z t),$$

$$I_{ft}\ddot{\theta}_{fx} = -I_{fp}\omega_z\dot{\theta}_{fy} - K_{frxx}(\theta_{fx} - \theta_{rx}) - C_{frx}(\dot{\theta}_{fx} - \dot{\theta}_{rx}) - K_{frxy}(\theta_{fy} - \theta_{ry}),$$

$$I_{ft}\ddot{\theta}_{fy} = I_{fp}\omega_z\dot{\theta}_{fx} - K_{fryy}(\theta_{fy} - \theta_{ry}) - C_{fry}(\dot{\theta}_{fy} - \dot{\theta}_{ry}) - K_{fryx}(\theta_{fx} - \theta_{rx}),$$

where d_2 is the distance between the flywheel and rotor mass centers with respect to the reference frame.

The e.o.m. of the rigid rotor are

$$M_r \ddot{x}_r = K_{mtxx}(x_m - x_r - d_1\theta_{ry}) + C_{mtx}(\dot{x}_m - \dot{x}_r - d_1\dot{\theta}_{ry})$$
$$+ K_{mtxy}(y_m - y_r + d_1\theta_{rx}) + K_{ftxx}(x_f - x_r - d_2\theta_{ry})$$
$$+ C_{ftx}(\dot{x}_f - \dot{x}_r - d_2\dot{\theta}_{ry}) + K_{ftxy}(y_f - y_r + d_2\theta_{rx})$$
$$- F_{n1}\cos(\alpha_1) + F_{t1}\sin(\alpha_1) - F_{n2}\cos(\alpha_2) + F_{t2}\sin(\alpha_2) + F_{sl},$$

$$M_r \ddot{y}_r = K_{mtyy}(y_m - y_r + d_1\theta_{rx}) + C_{mty}(\dot{y}_m - \dot{y}_r + d_1\dot{\theta}_{rx})$$
$$+ K_{mtyx}(x_m - x_r - d_1\theta_{ry}) + K_{ftyy}(y_f - y_r + d_2\theta_{rx})$$
$$+ C_{fty}(\dot{y}_f - \dot{y}_r + d_2\dot{\theta}_{rx}) + K_{ftyx}(x_f - x_r - d_2\theta_{ry})$$
$$- F_{n1}\sin(\alpha_1) - F_{t1}\cos(\alpha_1) - F_{n2}\sin(\alpha_2) - F_{t2}\cos(\alpha_2),$$

$$I_{rt}\ddot{\theta}_{rx} = -I_{rp}\omega_z\dot{\theta}_{ry} - d_1\lfloor K_{mtyy}(y_m - y_r + d_1\theta_{rx})$$
$$+ C_{mty}(\dot{y}_m - \dot{y}_r + d_1\dot{\theta}_{rx}) + K_{mtyx}(x_m - x_r - d_1\theta_{ry})\rfloor$$
$$- d_2[K_{ftyy}(y_f - y_r + d_2\theta_{rx}) + C_{fty}(\dot{y}_f - \dot{y}_r + d_2\dot{\theta}_{rx})$$
$$+ K_{ftyx}(x_f - x_r - d_2\theta_{ry})] + l_1[-F_{n1}\sin(\alpha_1)$$
$$- F_{t1}\cos(\alpha_1)] - l_2[-F_{n2}\sin(\alpha_2) - F_{t2}\cos(\alpha_2)]$$
$$+ K_{mrxx}(\theta_{mx} - \theta_{rx}) + C_{mrx}(\dot{\theta}_{mx} - \dot{\theta}_{rx})$$
$$+ K_{mrxy}(\theta_{my} - \theta_{ry}) + K_{frxx}(\theta_{fx} - \theta_{rx})$$
$$+ C_{frx}(\dot{\theta}_{fx} - \dot{\theta}_{rx}) + K_{frxy}(\theta_{fy} - \theta_{ry}),$$

$$I_{rt}\ddot{\theta}_{ry} = I_{rp}\omega_z\dot{\theta}_{rx} + d_1\lfloor K_{mtxx}(x_m - x_r - d_1\theta_{ry})$$
$$+ C_{mtx}(\dot{x}_m - \dot{x}_r - d_1\dot{\theta}_{ry}) + K_{mtxy}(y_m - y_r + d_1\theta_{rx})\rfloor$$
$$+ d_2[K_{ftxx}(x_f - x_r - d_2\theta_{ry}) + C_{ftx}(\dot{x}_f - \dot{x}_r - d_2\dot{\theta}_{ry})$$
$$+ K_{ftxy}(y_f - y_r + d_2\theta_{rx})] - l_1[-F_{n1}\cos(\alpha_1) + F_{t1}\sin(\alpha_1)]$$
$$+ l_2[-F_{n2}\cos(\alpha_2) + F_{t2}\sin(\alpha_2)] + K_{mryy}(\theta_{my} - \theta_{ry})$$
$$+ C_{mry}(\dot{\theta}_{my} - \dot{\theta}_{ry}) + K_{mryx}(\theta_{mx} - \theta_{rx})$$
$$+ K_{fryy}(\theta_{fy} - \theta_{ry}) + C_{fry}(\dot{\theta}_{fy} - \dot{\theta}_{ry}) + K_{fryx}(\theta_{fx} - \theta_{rx}),$$

$$I_p\ddot{\theta}_r = -(F_{t1} + F_{t2})\cdot R_r - T_{za},$$

where F_{n1} and F_{n2} are the radial normal contact forces between the rotor and CBs, F_{t1} and F_{t2} are the friction forces, l_1 and l_2 are the distances between the rotor mass center and CBs, and I_p is the polar moment of inertia of the total flywheel system.

From Fig. 2, the e.o.m. for the top CB are

$$M_{i1}\ddot{x}_{i1} = F_{n1}\cos(\alpha_1) - F_{t1}\sin(\alpha_1) - C_{b1}(\dot{x}_{i1} - \dot{x}_{o1}) - K_{b1}(x_{i1} - x_{o1}),$$
$$M_{i1}\ddot{y}_{i1} = F_{n1}\sin(\alpha_1) + F_{t1}\cos(\alpha_1) - C_{b1}(\dot{y}_{i1} - \dot{y}_{o1}) - K_{b1}(y_{i1} - y_{o1}),$$
$$M_{o1}\ddot{x}_{o1} = C_{b1}(\dot{x}_{i1} - \dot{x}_{o1}) + K_{b1}(x_{i1} - x_{o1}) + f_{sfx1},$$
$$M_{o1}\ddot{y}_{o1} = C_{b1}(\dot{y}_{i1} - \dot{y}_{o1}) + K_{b1}(y_{i1} - y_{o1}) + f_{sfy1},$$
$$I_b\ddot{\theta}_{b1} = F_{t1}\cdot R_b - T_{d1}.$$

The e.o.m. for the bottom CB are described as

$$M_{i2}\ddot{x}_{i2} = F_{n2}\cos(\alpha_2) - F_{t2}\sin(\alpha_2) - C_{b2}(\dot{x}_{i2} - \dot{x}_{o2}) - K_{b2}(x_{i2} - x_{o2}),$$
$$M_{i2}\ddot{y}_{i2} = F_{n2}\sin(\alpha_2) + F_{t2}\cos(\alpha_2) - C_{b2}(\dot{y}_{i2} - \dot{y}_{o2}) - K_{b2}(y_{i2} - y_{o2}),$$
$$M_{o2}\ddot{x}_{o2} = C_{b2}(\dot{x}_{i2} - \dot{x}_{o2}) + K_{b2}(x_{i2} - x_{o2}) + f_{sfx2},$$
$$M_{o2}\ddot{y}_{o2} = C_{b2}(\dot{y}_{i2} - \dot{y}_{o2}) + K_{b2}(y_{i2} - y_{o2}) + f_{sfy2},$$
$$I_b\ddot{\theta}_{b2} = F_{t2}\cdot R_b - T_{d2} + T_{za},$$

where $C_{b1,2}$ and $K_{b1,2}$ are the CB dampings and stiffnesses, $f_{sfx1,2}$ and $f_{sfy1,2}$ are the SFD forces including the o-ring stiffness to the X and Y directions, respectively and R_b is the CB bore radius. The bearing stiffness $K_{b1,2}$ is calculated according to the axial preload and inner race speed.

The axial model is developed as

$$M_m \ddot{z}_m = -K_{ma}(z_m - z_r) - C_{ma}(\dot{z}_m - \dot{z}_r) + M_m g,$$
$$M_f \ddot{z}_f = -K_{fa}(z_f - z_r) - C_{fa}(\dot{z}_f - \dot{z}_r) + M_f g,$$
$$M_r \ddot{z}_r = K_{ma}(z_m - z_r) + C_{ma}(\dot{z}_m - \dot{z}_r) + K_{fa}(z_f - z_r)$$
$$+ C_{fa}(\dot{z}_f - \dot{z}_r) - F_{cz} + M_r g,$$
$$M_i \ddot{z}_i = -K_{ba}(z_i - z_o) - C_{ba}(\dot{z}_i - \dot{z}_o) + F_{cz},$$
$$M_o \ddot{z}_o = K_{ba}(z_i - z_o) + C_{ba}(\dot{z}_i - \dot{z}_o) - K_{sa}z_o - C_{sa}\dot{z}_o,$$

where F_{cz} is the axial contact force between the rotor and bottom CB; K_{ba} is the axial stiffness of the bottom CB, which is also calculated according to the axial preload and inner race speed.

References

[1] T. Ishii, R.G. Kirk, Transient response technique applied to active magnetic bearing machinery during rotor drop, *Journal of Rotating Machinery and Vehicle Dynamics* 35 (1991) 191–199.
[2] R.G. Kirk, T. Ishii, Transient rotor drop analysis of rotors following magnetic bearing power outage, *Proceedings of MAG '93 Magnetic Bearings, Magnetic Drives, and Dry Gas Seals Conference & Exhibition*, Alexandria, VA, USA, 1993, pp. 53–61.
[3] R.G. Kirk, E.E. Swanson, F.H. Kavarana, X. Wang, J. Keese, Rotor drop test stand for AMB rotating machinery—part I: description of test stand and initial results, *Proceedings of the Fourth International Symposium on Magnetic Bearings*, Zurich, Switzerland, 1994, pp. 207–212.
[4] K. Ramesh, R.G. Kirk, Rotor drop test stand for AMB rotating machinery—part II: steady state analysis and comparison to experimental results, *Proceedings of the Fourth International Symposium on Magnetic Bearings*, Zurich, Switzerland, 1994, pp. 213–218.
[5] E.E. Swanson, R.G. Kirk, J. Wang, AMB rotor drop initial transient on ball and solid bearings, *Proceedings of MAG '95 Magnetic Bearings, Magnetic Drive and Dry Gas Seals Conference & Exhibition*, Alexandria, VA, USA, 1995, pp. 207–216.
[6] H.M. Chen, J. Walton, H. Heshmat, Test of a zero clearance auxiliary bearing, *Proceedings of MAG '97 Industrial Conference and Exhibition on Magnetic Bearings*, Alexandria, VA, USA, 1997, pp. 111–119.
[7] H. Xie, G.T. Flowers, Steady-state dynamic behavior of an auxiliary bearing supported rotor system, *American Society of Mechanical Engineers Winter Annual Meeting*, Chicago, USA, 1994, pp. 1–11.
[8] X. Wang, S. Noah, Nonlinear dynamics of a magnetically supported rotor on safety auxiliary bearings, *Journal of Vibration and Acoustics* 120 (1998) 596–606.
[9] M.O.T. Cole, P.S. Keogh, C.R. Burrows, The dynamic behavior of a rolling element auxiliary bearing following rotor impact, *Journal of Tribology* 124 (2002) 406–413.
[10] G. Sun, A. Palazzolo, A. Provenza, G. Montague, Detailed ball bearing model for magnetic suspension auxiliary service, *Journal of Sound and Vibration* 269 (2004) 933–963.
[11] Y.C. Shin, Bearing nonlinearity and stability analysis in high speed machining, *Journal of Engineering for Industry* 114 (1992) 23–30.
[12] B.R. Jorgensen, Y.C. Shin, Dynamics of machine tool spindle/bearing systems under thermal growth, *Journal of Tribology* 119 (1997) 875–882.
[13] K.H. Hunt, F.R.E. Crossley, Coefficient of restitution interpreted as damping in vibroimpact, *Journal of Applied Mechanics* (June 1975) 440–446.

[14] G. Sun, A High Fidelity Ball Bearing and Damper Model including Thermal Effects for Magnetic Suspension Auxiliary Service and Blade Loss Simulation, PhD Dissertation, Texas A&M University, 2003.

[15] K.H. Huebner, *The Finite Element Method for Engineers*, Wiley, New York, 1975.

[16] P.N. Bansal, D.H. Hibner, Experimental and analytical investigation of squeeze film bearing damper forces induced by offset circular whirl orbits, *Journal of Mechanical Design* (1978) 549–557.

[17] T.A. Harris, *Rolling Bearing Analysis*, second ed., Wiley-Interscience Publication, New York, 1984.

[18] S.P. Timoshenko, J.N. Goodier, *Theory of Elasticity*, third ed., McGraw-Hill, New York, 1987.

[19] J.L. Stein, J.F. Tu, A state-space model for monitoring thermally induced preload in anti-friction spindle bearings of high speed machine tools, *Journal of Dynamic Systems, Measurement, and Control* 116 (1994) 372–386.

[20] H. Aramaki, Y. Shoda, Y. Morishita, T. Sawamoto, The performance of ball bearings with silicon nitride ceramic balls in high speed spindles for machine tools, *Journal of Tribology* 110 (1988) 693–698.